Space Weather

RESEARCH ARTICLE
10.1029/2018SW002148

The Influence of Substorms on Extreme Rates of Change of the Surface Horizontal Magnetic Field in the United Kingdom

Mervyn P. Freeman[1], **Colin Forsyth**[2], **and I. Jonathan Rae**[2]

[1]British Antarctic Survey, Cambridge, UK, [2]Mullard Space Science Laboratory, University College London, Dorking, Surrey, UK

Key Points:
- We find that 54-56% of all extreme 1-min rates of change *R* of horizontal magnetic field in United Kingdom occur during substorm expansion and recovery phases
- Only 21-25% of large *R* during expansion and recovery phases are attributable to DP1 magnetic perturbation caused by substorm current wedge
- DP2 and substorm feedbacks on it may be dominant source of hazardous *R* (~>600 nT/min) that is potentially damaging to U.K. National Grid

Correspondence to:
M. P. Freeman,
mpf@bas.ac.uk

Citation:
Freeman, M. P., Forsyth, C., & Rae, I. J. (2019). The influence of substorms on extreme rates of change of the surface horizontal magnetic field in the United Kingdom. *Space Weather*, *17*. https://doi.org/10.1029/2018SW002148

Received 20 DEC 2018
Accepted 3 MAY 2019
Accepted article online 18 MAY 2019

Abstract We investigate how statistical properties of the rate of change *R* of the surface horizontal magnetic field in the United Kingdom differ during substorm expansion and recovery phases compared with other times. *R* is calculated from 1-min magnetic field data from three INTERMAGNET observatories —Lerwick, Eskdalemuir, and Hartland and between 1996 and 2014—nearly two solar cycles. Substorm expansion and recovery phases are identified from the SuperMAG Lower index using the Substorm Onsets and Phases from Indices of the Electrojet method. The probability distribution of *R* is decomposed into categories of whether during substorm expansion and recovery phases, in enhanced convection intervals, or at other times. From this, we find that 54–56% of all extreme *R* values (defined as above the 99.97th percentile) occur during substorm expansion or recovery phases. By similarly decomposing the magnetic local time variation of the occurrence of large *R* values (>99th percentile), we deduce that 21–25% of large *R* during substorm expansion and recovery phases are attributable to the Disturbance Polar (DP)1 magnetic perturbation caused by the substorm current wedge. This corresponds to 10–14% of all large *R* in the entire data set. These results, together with asymptotic trends in occurrence probabilities, may indicate the two-cell DP2 magnetic perturbation caused by magnetospheric convection as the dominant source of hazardous $R > 600$ nT/min that is potentially damaging to the U.K. National Grid. Thus, further research is needed to understand and model DP2, its mesoscale turbulent structure, and substorm feedbacks in order that GIC impact on the National Grid may be better understood and predicted.

1. Introduction

Electricity supply networks, such as the U.K.'s National Grid, can be adversely affected by geomagnetically induced currents (GIC; e.g., Cannon et al., 2013; Erinmez et al., 2002; Love et al., 2018; Rodger et al., 2017; Thomson et al., 2005). A GIC is driven in the conducting Earth (Thomson & Weaver, 1975) and grounded electricity supply network (Lehtinen & Pirjola, 1985) by an electric field that is induced by temporal variations in the surface magnetic field. These magnetic variations are caused by changes in electrical currents flowing in the ionosphere and further out in space.

While the detailed properties of GICs will thus depend on the structure and interactions of the inducing currents, ground conductivity, and network components (e.g., Beggan, 2015; Erinmez et al., 2002; Thomson et al., 2005; Viljanen et al., 1999), a necessary condition for any potentially damaging GIC is a large rate of change of the horizontal component of the surface magnetic field $\partial\mathbf{H}/\partial t$ (Viljanen et al., 2001). As a guide to what may constitute "potentially damaging" and "large," Thomson et al. (2005) report that sustained GICs above about 25 A are of potential concern to the U.K. National Grid engineers. And Thomson et al. (2005) showed that measured GIC fluctuations transiently exceeding this level could be reasonably reproduced from surface magnetic field data less than 100 km away in which $\partial H/\partial t$ from 1-s data reached about 10 nT/s or equivalently about 600 nT/min (if sustained).

Consequently, it is useful to assess the return periods of extreme $\partial H/\partial t$ (Nikitina et al., 2016; Thomson et al., 2011) and to understand the physical sources of large $\partial\mathbf{H}/\partial t$ with a view to their prediction. In general, the strongest surface magnetic field perturbations occur during geomagnetic storms. (This is almost by definition if storms are identified using indices such as *aa*, A_p, or K_p that are derived from the range of surface magnetic field variations, although the conventional definition of a storm is based on the Dst index which is not based on range; e.g., Love & Gannon, 2009, and references therein.) Geomagnetic storms are

typically caused by corotating interaction regions or coronal mass ejections originating from the Sun (Borovsky & Denton, 2006), whose arrival is potentially predictable from solar and interplanetary observations (e.g., Harrison et al., 2017; Zhao & Dryer, 2014). However, understanding and predicting consequent surface magnetic field perturbations is challenging, even if the all-important state of the interplanetary magnetic field (IMF) is known. For example, in a study of how well first principles and empirical models can reproduce 1-min surface magnetic field variations during four storms (Pulkkinen et al., 2011), the so-called prediction efficiencies of the models were typically no better than assuming the average observed perturbation over the storm rather than the model prediction. (The prediction efficiency is defined as the ratio of the sum squared difference between the observed and modeled surface magnetic field over a storm to the variance of the observed field.)

An important source of uncertainty in predicting surface magnetic field variations comes from the strong and dynamic ionospheric currents generated by substorms. A substorm is a cycle of energy storage and release within the magnetosphere that comprises three phases—growth, expansion, and recovery (Akasofu, 1964; McPherron, 1970; McPherron et al., 1973): (1) The growth phase lasts ~1 hr during which the IMF orientation is favorable (i.e., predominantly southward) for reconnection at the magnetopause to be sustained. This creates open magnetic flux, which is advected into the magnetotail lobes. The lobe magnetic field strength and hence magnetic pressure increase, causing an increase of the total pressure in the central plasma sheet (Forsyth et al., 2014). The associated increase in magnetotail energy and cross-tail current continues until some point of instability known as substorm onset (e.g., Kalmoni et al., 2015, 2017, 2018). (2) Following onset, the expansion phase lasts about 20 min during which the cross-tail current is diverted into the ionosphere to form a substorm current wedge (SCW), the aurora brightens, the magnetic field relaxes toward a dipolar configuration, and closed and then open magnetic flux is reconnected forming a plasmoid (Hones, 1979). The expansion phase releases magnetic energy (e.g., Coxon et al., 2018) through Joule heating of the thermosphere (e.g., Tanskanen et al., 2002) and particle precipitation into it (e.g., Ostgaard et al., 2002), the enhancement of particle energy in the ring current (e.g., Sandhu et al., 2018), and the ejection of the plasmoid downtail. (3) Finally, the recovery phase lasts 2–3 hr during which the substorm currents decay and energy continues to be lost from the system by Joule heating and particle precipitation into the atmosphere.

The substorm is imperfectly and inconsistently represented in first principles models (Gordeev et al., 2017), which contributes to the aforementioned poor prediction of the surface magnetic field. Only limited prediction of the timing and size of substorms has so far been possible. Substorms in corotating interaction region- and coronal mass ejection-driven storms tend to recur quasi-periodically on a time scale of 2–4 hr (Huang et al., 2004; Lee et al., 2006). In these cases, Morley et al. (2009) suggest some predictability of individual onsets if not amplitudes. More generally, only the statistics of substorm recurrence and amplitude have been successfully reproduced, rather than individual substorm onset times and sizes (Freeman & Morley, 2004; Morley et al., 2007).

The general inability to predict individual substorms appears problematic to protecting electricity supply networks because there is evidence that substorms influence $\partial\mathbf{H}/\partial t$ and hence GICs: First, GIC occurrence in Finland maximizes around midnight magnetic local time (MLT; Viljanen et al., 2001), which is where the Disturbance Polar 1 (DP1) surface magnetic field perturbation associated with the SCW is concentrated (e.g., Shore et al., 2018). Second, DP1 is found to be the third greatest contributor to the total variance of the surface magnetic field in winter, based on a decomposition of the surface magnetic field variation into a set of empirical orthogonal functions (EOFs; analogous to Fourier decomposition; Shore et al., 2018). The DP1 EOF and three other EOFs describing DP1 evolution can contribute about a fifth of the total variance (Shore et al., 2017). Third, the time of the maximum $\partial\mathbf{H}/\partial t$ observed between 20 min before substorm onset to 60–90 min afterward peaks within a few minutes after the onset (Turnbull et al., 2009; Viljanen et al., 2006).

However, $\partial\mathbf{H}/\partial t$ can also be caused by other current sources, and these may be more predictable. From the EOF analysis of Shore et al. (2018), we know the following: The leading contributor to the surface horizontal magnetic field variance in any given month over a solar cycle is the DP2 magnetic disturbance (Nishida, 1968a, 1968b) associated with the global convection cycle (Dungey, 1961). DP2 is characterized by its two-cell spatial structure and its variable but near-continuous presence. Typically, 20–50% of the DP2

Table 1
Coordinates of the U.K. INTERMAGNET Observatories

Observatory	Geographic latitude (°N)	Geographic longitude (°E)	Corrected geomagnetic latitude (°N)	Corrected geomagnetic longitude (°E)
LER	60.138	358.817	58.0	80.7
ESK	55.314	356.794	52.6	77.0
HAD	50.995	355.516	47.5	74.5

Note. Corrected geomagnetic coordinates are given for the year 2005. LER = Lerwick; ESK = Eskdalemuir; HAD = Hartland.

contribution is explained by the north-south component of the IMF. In summer months, the second most important contributor to monthly surface horizontal magnetic field variance is the single-cell DPY magnetic disturbance (Friis-Christensen & Wilhjelm, 1975) that creates a dawn-dusk asymmetry in DP2. Typically, 25–65% of the DPY contribution is explained by the east-west component of the IMF. In other months, the second most important contributor describes the expansion and contraction of DP2 (Lockwood et al., 1990) and has been termed DP2EC by Shore et al. The DP2EC contribution is poorly explained (<20% of its variance) by the IMF vector, as is DP1.

In summary, while substorms do appear to influence $\partial\mathbf{H}/\partial t$ and GICs, it is unclear just how important the DP1 magnetic disturbance caused by substorms is. Consequently, explicit comparisons are needed of the relative likelihood of potentially hazardous $\partial\mathbf{H}/\partial t$ during the substorm expansion and recovery phases compared to other times and of the relative importance of DP1, DP2, and other sources. Here, we make these comparisons by analyzing surface magnetic field variations in the United Kingdom over more than one solar cycle. In section 2 we introduce the data sources and the general statistical methodology for analyzing them and testing for substorm dependencies. In section 3 we present the results factually with minimal physical interpretation. In section 4 we interpret the results in terms of the substorm and other physical influences on large $\partial\mathbf{H}/\partial t$. In section 5 we summarize our main conclusions.

2. Method

2.1. Magnetometer Data

We analyze magnetometer data from the three INTERMAGNET observatories located in the United Kingdom and operated by the British Geological Survey. The observatories are Lerwick (LER), Eskdalemuir (ESK), and Hartland (HAD) at geographic and geomagnetic coordinates given in Table 1. As shown in Figure 1, these magnetometers straddle the United Kingdom and the National Grid.

The time interval of the analysis is from 1996 to 2014 inclusive (hence, the choice of 2005 as the central year for calculating the geomagnetic coordinates given in Table 1). This interval begins with the solar minimum at the start of solar cycle 23 in 1996 (annual average sunspot number $\overline{S} = 12$). It goes through solar maximum around 2000 ($\overline{S} = 174$) to the very low and prolonged solar minimum around 2009 ($\overline{S} = 5$) at the start of solar cycle 24. It then ends just after the weaker solar maximum around 2013 ($\overline{S} = 94$).

2.2. Rate of Change Estimation

We analyze the rate of change R of the horizontal surface magnetic field vector $\mathbf{H} = (X,Y)$, where X and Y are the geographic northward and eastward components

$$R = \frac{|\delta\mathbf{H}|}{\delta t} = \frac{\sqrt{[X(t+\delta t)-X(t)]^2 + [Y(t+\delta t)-Y(t)]^2}}{\delta t} \quad (1)$$

That is, R is the absolute displacement of the vector $\mathbf{H}$ per unit time between times t and $t+\delta t$ (e.g., Viljanen et al., 2001), rather than, for example, the rate of change of the vector magnitude $dH/dt = d|\mathbf{H}|/dt$ (Thomson et al., 2011). Taking the directional change in $\mathbf{H}$ into account may be important because it can be very variable (e.g., Viljanen et al., 2001) and the GICs produced in an electricity supply network depend on its relative orientation to the inducing field (e.g., Beggan, 2015). For the INTERMAGNET data used here, $\delta t = 1$ min is

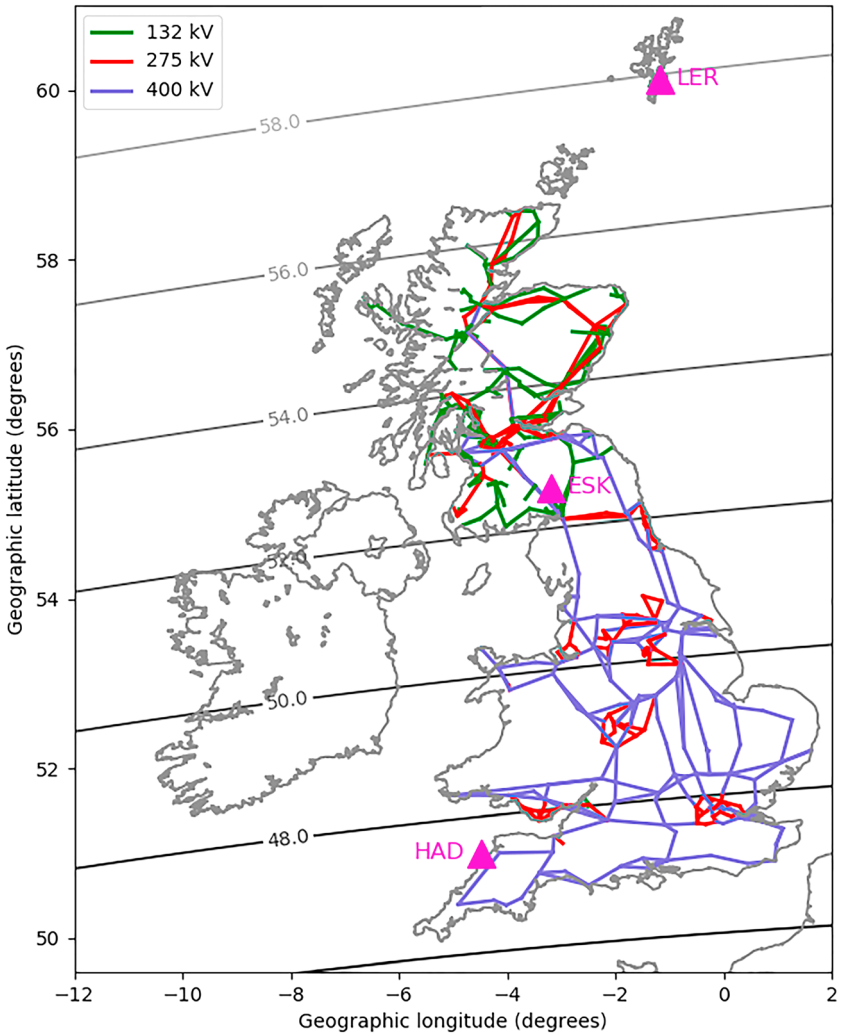

Figure 1. A map of the United Kingdom and Ireland, and part of France, showing the Lerwick (LER), Eskdalemuir (ESK), and Hartland (HAD) magnetic observatories (magenta triangles) with respect to the high-voltage transmission lines (in blue, red, and green) of the U.K. National Grid.

the separation in time between samples and each sample is a 1-min average centered on the universal time coordinated (UTC) minute (e.g., t = 01:39:00 UTC is the average between 01:38:30 UTC and 01:39:29 UTC). We will use the variable R for the measure defined using equation (1) and 1-min INTERMAGNET data and reserve $\partial\mathbf{H}/\partial t$ as the abbreviation for the rate of change of the horizontal component of the surface magnetic field vector in general.

2.3. Probability Density Estimation

A statistical distribution is defined by its probability density (or probability per unit range of R), which can be estimated by

$$p_i(R) = \frac{n_i}{N\Delta} \tag{2}$$

where n_i is the number of samples in the ith bin (i = 1,2,3,...), N is the total number of samples, and Δ is the width of the bin. Since, as we shall see, the probability density function (PDF) has a heavy tail (i.e., tends to zero slower than an exponential), we shall use nonuniform bins that are monotonically increasing in width. This is because a given constant bin width would be either too small in the tail or too large in the bulk of the distribution to adequately estimate the PDF. In the former case, it is difficult to assess the shape of the tail

because many bins have zero or few counts and hence relatively large statistical uncertainty. In the latter case, only a few bins would cover the bulk of the distribution.

In what follows, we shall use bins that are algebraically increasing in width and hence evenly spaced in log$R$. That is, we count the frequency n_i of $\log_{10}R$ in evenly spaced bins with centers at $\log_{10}R_c = \log_{10}(R_{\min}) + (i - 1/2)\log_{10}(w)$, where $i = 1,2, \ldots, N_{\text{bin}} - 1$ is the index of the bin, $R_{\min}$ is the left-hand edge of the first bin, and $\log_{10}(w)$ is the bin width in log$R$ space. The magnetometer measurements have an amplitude resolution of 0.1 nT in each cardinal direction (St-Louis, 2012), and so $|\delta\mathbf{H}|$ is quantized in units of $0.1\sqrt{j^2 + k^2}$ where $j,k \in \{0,1,2,\ldots\}$. Thus, we choose values of $R_{\min} = 0.09$ nT and $w = 1.4$ to ensure that at least one quantized value lies in each of the bins. In this case, the bin centers are at $R_c = 0.09(1.4)^{(i\ -\ 1/2)}$ nT/min and the bin width $\Delta = 0.036(1.4)^{(i\ -\ 1)}$ nT/min. We also choose $N_{\text{bin}} = 28$ to encompass all nonzero values of R at the three observatories for 1996–2014; the maximum measured value being $R = 710$ nT/min at LER at 21:19 UTC on 30 October 2003.

Lastly, samples where R is less than the 0.1-nT quantization value are all recorded in the INTERMAGNET data set as $R = 0$ and hence $\log R \to -\infty$. Consequently, we define a bin $i = 0$ between zero and $R_{\min}$ and centered at $R_{\min}/2$ with probability density

$$p_0(R) = \frac{n_0}{NR_{\min}} \tag{3}$$

In this way, these R values are properly included in the PDF even though their values are not precisely known.

Error bars on the PDF value for each bin are estimated for a given confidence interval, defined as the proportion of times that the experimental result would be within the corresponding error bars if the experiment were repeated many times. Following Gehrels (1986), the observed frequency in a given bin n_i is independently and identically distributed according to a Poisson distribution. This tends to a normal distribution for sufficiently large n_i, in which case the 68.27% confidence interval corresponds to ± 1 standard deviation and the error bars are the familiar $\pm\sqrt{n_i}$ (to within a few percent for $n_i > 100$). However, for smaller frequencies the error bars deviate from this approximation and are asymmetric. Thus, we calculate error bars for the 68.27% confidence interval assuming the general Poisson distribution using the tabulated values provided by Gehrels (1986).

2.4. Substorm Phase Identification

The aim of this paper is to investigate how the statistical distribution of R is affected by substorm phase and in particular to ask whether the most extreme R associated with potentially damaging GIC preferentially occurs in the expansion and recovery phases following substorm onset. The phases have been identified using the Substorm Onsets and Phases from Indices of the Electrojet (SOPHIE) technique devised by Forsyth et al. (2015). Briefly, the technique estimates the time derivative of the 30-min low-pass filtered SuperMAG Lower index (*SML*; Gjerloev, 2012) and then separately finds the percentiles of the positive derivative and of the magnitude of the negative derivative. A negative derivative whose magnitude is above a given expansion phase threshold percentile (*EPT*) is deemed to be in an expansion phase and a positive derivative above a given recovery phase threshold percentile is within a recovery phase. Any other time is identified as being within a "possible growth phase." Resulting short phases (typically less than 30 min) that occur apparently out of order in the expected growth-expansion-recovery phase sequence are then reclassified as one of the surrounding phases. This algorithm is then repeated for the same *EPT* but varying recovery phase threshold percentile until the number of expansion and recovery phases are most similar. After this, the start of each expansion phase is adjusted using the time derivative of the unfiltered *SML*.

EPT is thus a free parameter. Decreasing *EPT* will increase the number of intervals identified as expansion phases (and similarly recovery phases). In this study we use $EPT = 90\%$, which identifies most substorm onsets (see section 4.1) and provides a conservative estimate of the amount of time spent in the expansion and recovery phases (4.1% and 9.3%, respectively). We choose to be conservative because if we find (as we indeed do below) that instances of large R dominantly occur during the expansion and recovery phases, then this result will also stand (and even more dominantly) if *EPT* was reduced.

In the SOPHIE method, expansion and recovery phases are additionally subdivided into two classes based on the typical rate of change of *SML* over the expansion phase compared to that of the SuperMAG Upper index (*SMU*). Denoting d*X* as the 1-min change in *X*, then a test is made of whether either the mean or median of |d*SML*|/|d*SMU*| over the expansion phase is less than 2. If the test result is true, then the expansion phase and subsequent recovery phase identified by SOPHIE are reclassified as an enhanced convection interval instead. Physically, this is interpreted as an implied relatively symmetric enhancement of the eastward and westward auroral electrojets that is indicative of an enhancement of DP2 rather than DP1. In this case, enhanced convection intervals are not substorms, and so we will consider them here as separate from the other expansion and recovery phases. (The percentages given in the previous paragraph assume this.)

In summary, using the SOPHIE method, we divide all *R* values into four categories according to whether they occur during the expansion phase, recovery phase, enhanced convection interval, or possible growth phase. Henceforth, we will use "other times" rather than possible growth phase because growth phase typically implies an interval of increasing magnetotail magnetic flux and it is unclear that this is always so in the possible growth phase category, for example, at very quiet times and/or many hours before a substorm onset.

2.5. Definition of Large, Extreme, and Hazardous Rates of Change

Finally, as mentioned above, we are most interested in the dependence on substorm phase of values of *R* that are potentially hazardous to the National Grid. In section 1, we suggested that this may correspond to sustained $\partial H/\partial t > 10$ nT/s. Thus, here, we shall define hazardous *R* as values exceeding 600 nT/min, recognizing that this is only a rough guide. In our 19-year magnetometer data set, *R* exceeded 600 nT/min on only 4, 2, and 0 occasions at LER, ESK, and HAD, respectively, during 1996 to 2014; the exceedances being on either 29 or 30 October 2013 during the so-called "Halloween" storm (e.g., Thomson et al., 2005). So hazardous *R* is too rare to statistically conclude any substorm dependence from these samples alone. Yet hazardous *R* is sufficiently frequent to be relevant to electricity infrastructure management and planning; an extreme value analysis (Thomson et al., 2011) estimates the return period of a 600-nT/min value to be 10–30 years at ESK.

Consequently, we shall examine how the probability of *R* depends on substorm phase over a sufficient range of the tail of the probability distribution that any identified dependence may reasonably be extrapolated beyond the observed limit. In this context, we shall follow Thomson et al. (2011) and use the term extreme *R* for values of *R* exceeding the quantile *E* corresponding to the 99.97th percentile. This is because, in extreme value theory, the asymptotic distribution of the tail of a wide range of distributions tends to the generalized Pareto distribution $F(x) = 1 - (1+Kx/\sigma)^{-1/K}$, where the exceedance $x = R - E > 0$ and K and σ are the shape and scale parameters, respectively. Thomson et al. (2011) found that this tendency occurred at the 99.97th percentile of *R* at ESK and most other European INTERMAGNET observatories that they studied. Hence, this percentile defines extreme values in this sense. The value of *R* at the 99.97th percentile is $E = 66$ nT/min for LER, 41 nT/min for ESK, and 20 nT/min for HAD.

We shall also use the term large *R* for values above the 99th percentile, corresponding to 8.5 nT/min for LER, 6.8 nT/min for ESK, and 4.2 nT/min for HAD.

3. Results

3.1. Variation of Large and Extreme *R* With Time

In order to set the following substorm dependence results in context, Figure 2 summarizes the occurrence of large and extreme *R* in each Carrington rotation (CR) over our study interval 1996–2014 for (a) LER, (b) ESK, and (c) HAD. For reference, the first rotation shown is CR 1905, which starts at 01:25 UTC on 17 January 1996, and the last is CR 2157, which ends at 14:35 UTC on 8 December 2014. The vertical guidelines show the times of the solar maxima (dashed) in solar cycle 23 and solar cycle 24 and the intervening solar minimum (dotted). These were defined from the monthly mean sunspot number whose maxima occurred in July 2000 (CR 1964–1965) and February 2014 (CR 2146–2147) and the minimum occurred in August 2009 (CR 2086–2087).

The top row of Figure 2 shows the CR probability and 68.27% confidence interval error bars. The CR probability is the probability of occurrence of a large *R* (blue) and extreme *R* (orange) value in a given rotation. Also shown is a 13-rotation running mean of this probability for large *R* (black), corresponding to an

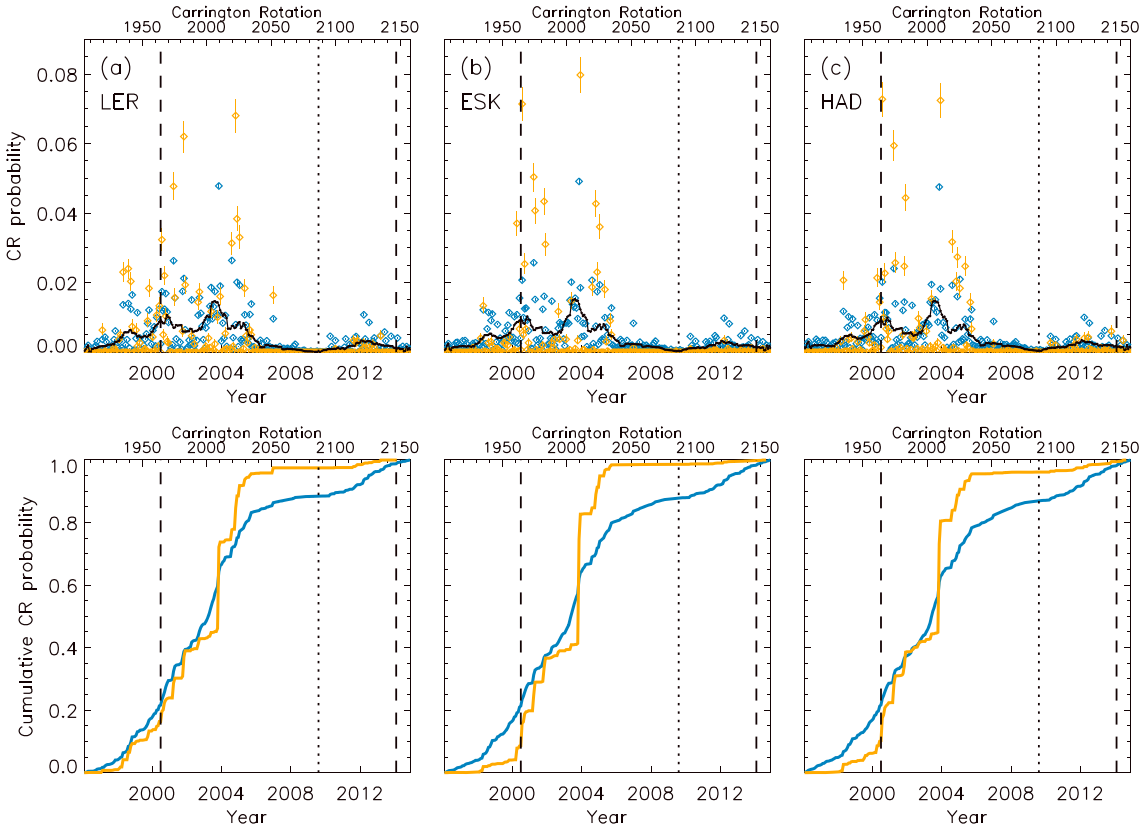

Figure 2. Occurrence of large and extreme *R* in each Carrington rotation (CR) over years 1996–2014 for (a) LER, (b) ESK, and (c) HAD. Top row shows the CR probability—the probability of occurrence of large *R* (blue) and extreme *R* (orange) in a given rotation,and a 13-rotation running mean of the large *R* probability (black). The lower horizontal axis is the year and the upper axis is the CR number. Bottom row shows the corresponding cumulative probabilities with the same horizontal axes. For reference, the first rotation shown is CR 1905, which starts at 01:25 UTC on 17 January 1996, and the last is CR 2157, which ends at 14:35 UTC on 8 December 2014. The vertical dashed guidelines show the times of the solar maxima (dashed lines) in solar cycle 23 and solar cycle 24 and the intervening solar minimum (dotted line), defined from the monthly mean sunspot number.

approximately annual smoothing. There is considerable rotation-to-rotation variation but with a clear solar cycle modulation, peaking in the declining phase after solar cycle 23 maximum.

The bottom row of Figure 2 shows the corresponding cumulative probability of large *R* (blue) and extreme *R* (orange) lying in each CR, from which it can be more readily seen that the vast majority of extreme *R* (81%, 90%, and 86% for LER, ESK, and HAD, respectively) occur between solar cycle 23 maximum and the following minimum. The majority of large *R* occur over this interval too (67%, 67%, and 66% for LER, ESK, and HAD, respectively). Also evident is a rapid jump in the cumulative probability at all three stations in CR 2009 between 13:03 UT, 23 October 2003 and 20:20 UT, 19 November 2003. This rotation includes the Halloween storm and contains 26%, 33%, and 28% of all the extreme *R* values at LER, ESK, and HAD, respectively (and an additional ~7–8% in the next rotation at ESK and HAD). The probabilities for rotation 2009 are in fact off scale in the probability plots (Figure 2 top row). However, the Halloween storm is not such a dominant contributor to large *R* (5% at all three stations).

3.2. Parent Distribution

Figure 3 shows the PDFs of *R* for LER (black), ESK (orange), and HAD (blue) for the interval 1996–2014 inclusive in which only 81, 11, and 4 samples, respectively, were missing out of the 9,993,599 maximum possible. Using the same station color coding, the vertical guidelines show, from left to right, the 90th percentiles (dotted), the 99th percentiles (dashed) that we have used to define large *R*, and the 99.97th percentiles (long dashed) defining extreme *R*. The distribution tail above about the 90th percentile falls off rapidly (roughly $\sim R^{-3}$ at ESK) and increasingly so with decreasing CGM latitude as is evident from the divergence of the PDF tail with increasing *R* at the three stations.

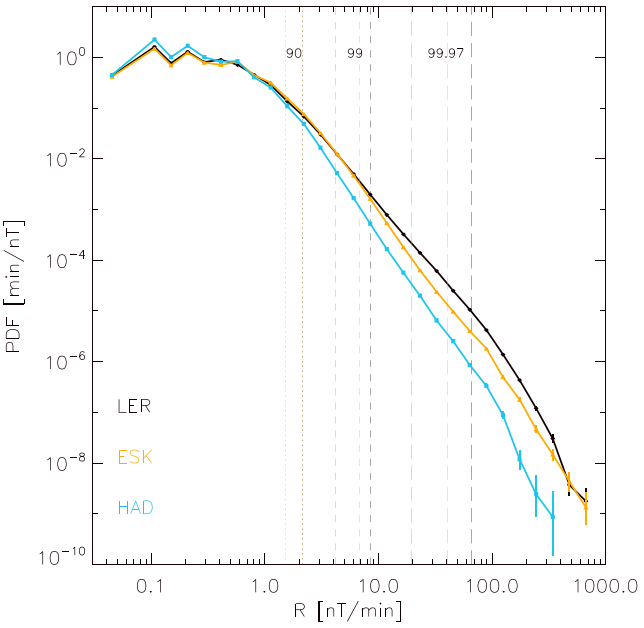

Figure 3. The PDFs of *R* for the LER (black), ESK (orange), and HAD (blue) magnetic observatories for the interval 1996–2014 inclusive. Using the same station color coding, the vertical guidelines show, from left to right, the 90 (dotted), 99 (dashed), and 99.97 (long dashed) percentiles of each distribution. (The 90th percentile at LER is hidden because it is virtually the same as at ESK.) PDF = probability density function; LER = Lerwick; ESK = Eskdalemuir; HAD = Hartland.

3.3. Substorm Phase Distributions

The top row of Figure 4 presents again the PDFs of all *R* values for (a) LER, (b) ESK, and (c) HAD for the interval 1996–2014 inclusive, in a similar format to Figure 3. These total PDFs are shown in black. For each panel, superposed are the partial PDFs for *R* values identified to occur in the substorm expansion phase (sky blue), recovery phase (purple), enhanced convection interval (green), and at other times (i.e., the so-called possible growth phase; orange). That is, for each station, the sum of these four PDFs gives the total PDF. For all three stations, extreme *R* values (i.e., above the 99.97th percentile—long dashed vertical guideline) occur more often in the expansion and recovery phases than at other times and also more often in enhanced convection intervals than at other times.

To show this more clearly, and to quantify how much more often, the lower panels of Figure 4 show the percentage proportion of all *R* values in each bin that occur in the expansion phase (sky blue), recovery phase (purple), enhanced convection interval (green), at other times (thick orange), and in the expansion and recovery phases combined (thick blue). Proportions based on frequencies less than 25 are not joined by a continuous curve as these will have significant uncertainties (>20%). It can be seen that the proportion of *R* values occurring in the expansion and recovery phases, as well as during enhanced convection intervals, increases as *R* increases, while consequently the proportion during other times decreases with increasing *R*. Comparing the two thick curves, *R* values at the extreme threshold (i.e., 99.97th percentile) are twice as likely to occur in expansion and recovery phases combined than at other times at HAD and five times more likely at LER.

Values of *R* at both the large and extreme thresholds (i.e., dashed and long dashed vertical guidelines) occur about half the time in the combined expansion and recovery phases. Integrating the PDF above the large threshold, we find that 55% of large *R* at LER occur during the substorm expansion and recovery phases combined, compared with 19% during enhanced convection intervals and 27% other times. For ESK these percentages are 49%, 16%, and 35%, respectively, and at HAD they are 49%, 15%, and 36%. Similarly, we find that 56% of extreme *R* at LER occur during the substorm expansion and recovery phases combined, compared with 32% during enhanced convection intervals and 12% other times. For ESK these percentages are 54%, 32%, and 14%, respectively, and at HAD they are 54%, 30%, and 16%. Note that the substorm-related percentages are likely to be an underestimate because of the conservative expansion phase threshold, $EPT = 90$, that we have used in the SOPHIE technique.

The preponderance of large and extreme *R* values during the expansion and recovery phases combined is despite the fact that these phases account for a minority of all data (13.4%). Thus, in Figure 5 we present the *R* occurrence in a different way: Rather than the partial PDFs considered in Figure 4, the top row of Figure 5 now compares the PDFs calculated for each phase separately, that is, normalized by the number of samples in each phase rather than by the total number of samples. This then is the probability density of *R* given a particular phase. As before, the PDF for all *R* values is shown in black. Above the 90th percentile (dotted vertical guideline), we see that *R* values are more likely than this overall PDF in the expansion phase (sky blue), recovery phase (purple), and enhanced convection (green) and less likely during other times (orange).

In the respective lower panels of Figure 5 are then shown the ratios of the PDF in the expansion phase (sky blue), recovery phase (purple), enhanced convection (green), and other times (orange) with respect to the overall PDF. Similar to Figure 4, ratios based on frequencies less than 25 are not joined by a continuous curve to indicate their relatively large uncertainty. For large *R* above the 99th percentile (dashed vertical guideline), *R* values in the expansion phase are about five times more likely to occur than overall and about three times more likely in the recovery phase. Also shown are the ratios of the PDF in the expansion and recovery phases combined (thick blue) and in enhanced convection intervals (thick green) with respect to the PDF at

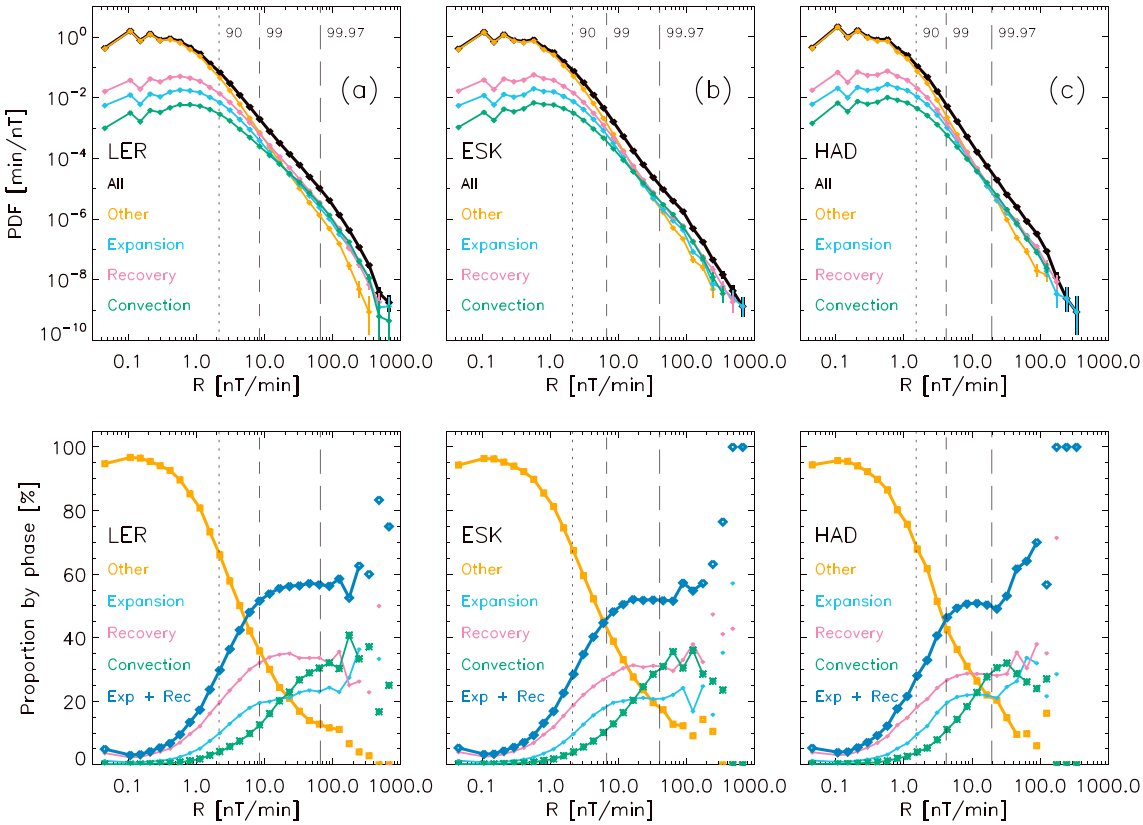

Figure 4. (a–c) Top row: The partial PDFs of *R* for the LER, ESK, and HAD magnetic observatories for the interval 1996–2014 inclusive from the expansion phase (sky blue), recovery phase (purple), enhanced convection (green), other times (orange), and overall (black). Bottom row: The proportion of the overall PDF at each value of *R* contributed by the expansion phase (sky blue), recovery phase (purple), enhanced convection (green), other times (thick orange), and by the expansion and recovery phases combined (thick blue). The vertical guidelines in each of the panels show, from left to right, the 90 (dotted), 99 (dashed), and 99.97 (long dashed) percentiles of the total distribution. PDF = probability density function; LER = Lerwick; ESK = Eskdalemuir; HAD = Hartland.

other times. This shows that at the 99th percentile, *R* values in the expansion and recovery phases combined are 8–10 times more likely to occur than during other times (depending on station), and this increases to at least 10–30 times more likely for extreme *R* above the 99.97th percentile (long dashed vertical guideline). The PDF ratios for enhanced convection intervals are even higher, with extreme *R* being over 10 times more likely than overall and over 100 times more likely than at other times.

3.4. MLT Variation

Lastly, we analyze how the occurrence of large *R* varies with MLT. The top row of Figure 6 shows the probability of *R* being above the 99th percentile as a function of MLT for (a) LER, (b) ESK, and (c) HAD. As before, we show the probability for all values in the sample (black) and for the subsets in the expansion phase (sky blue), recovery phase (purple), enhanced convection (green), at other times (orange), and in the expansion and recovery phases combined (blue).

For LER it is evident that the probability of large *R* (black) has a broad peak between 19 and 01 MLT and that this mainly arises from an increased probability of large *R* centered on 22 MLT during the expansion and recovery phases combined (blue). In contrast, the probability of large *R* (black) at both ESK and HAD has two peaks—one at 8 MLT and another more complicated one at 16 MLT or later. This MLT structure arises mainly from that of the expansion and recovery phases combined (blue) which peaks near 8 MLT and premidnight, but it is also influenced by the MLT variation of large *R* at other times (orange). The probability of large *R* during enhanced convection (green) is relatively minor and varies more smoothly than the other phases but once again seems more similar at ESK and HAD than at LER in the sense that it peaks around 24 MLT at LER but premidnight at ESK and HAD.

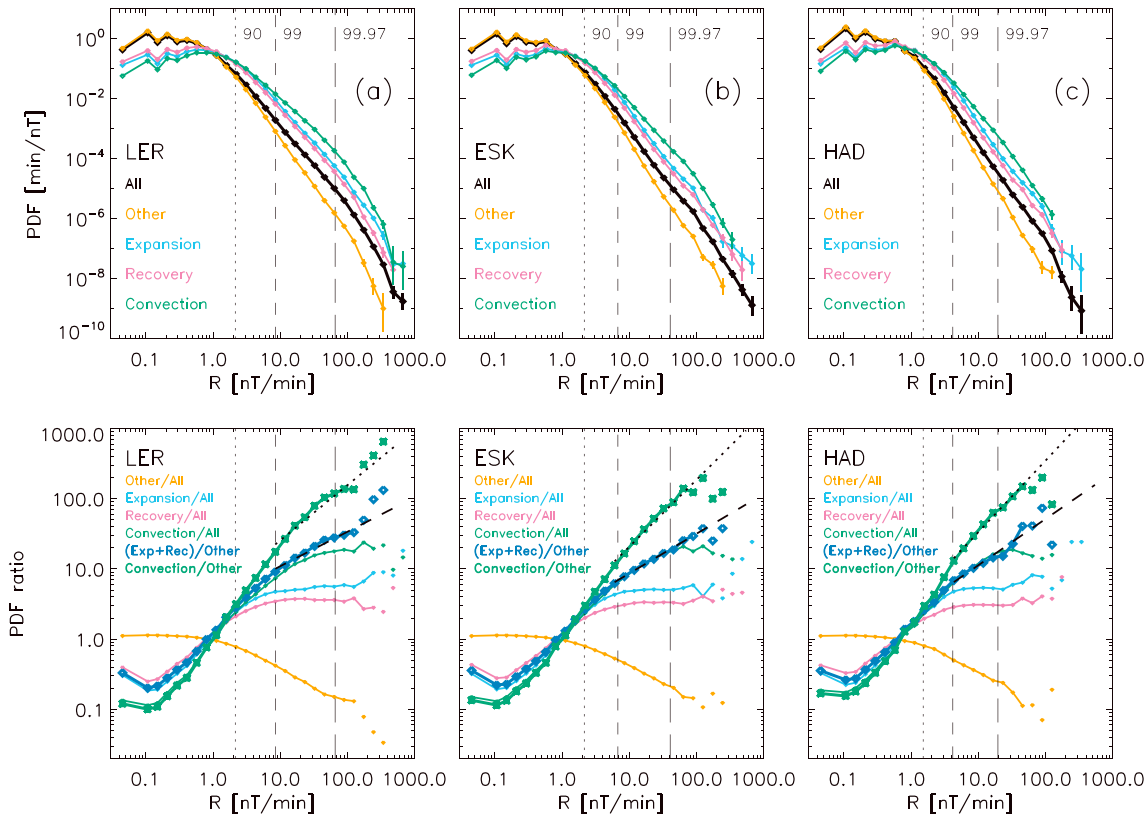

Figure 5. (a–c) Top row: The PDFs of *R* for the LER, ESK, and HAD magnetic observatories for the interval 1996–2014 inclusive for the expansion phase (sky blue), recovery phase (purple), enhanced convection (green), other times (orange), and overall (black). Bottom row: The ratio of the PDF at each value of *R* from the expansion phase (sky blue), recovery phase (purple), enhanced convection (green), and other times (orange) to the overall PDF. Also shown is the ratio of the PDF of *R* from the expansion and recovery phases combined to that from other times (thick blue) and from enhanced convection intervals to that from other times (thick green). For these latter two ratios, the dashed and dotted slanted lines respectively show possible asymptotic trends, derived from best fit power laws between large and extreme *R*. The vertical guidelines in each of these three panels show, from left to right, the 90 (dotted), 99 (dashed), and 99.97 (long dashed) percentiles of the total distribution. PDF = probability density function; LER = Lerwick; ESK = Eskdalemuir; HAD = Hartland.

Comparing the probability of large *R* during the expansion and recovery phases combined (blue) with that at other times (orange), we see that they are quite similar at ESK and HAD between 6 and 15 MLT. This suggests that the effect on large *R* following substorm onset is mainly an enhancement in occurrence on the nightside at these two stations, which seems reasonable given the known formation of the SCW and associated DP1 magnetic disturbance. In fact, a nightside enhancement in the probability of large *R* is seen at all three stations following onset in the sense that the probability variation with MLT during the expansion and recovery phases combined diverges from that at other times in the premidnight sector.

To clarify and evaluate this, in the lower panels we decompose the probability during the expansion and recovery phases combined (blue) into two components. The first component (orange) is simply proportional to the probability at other times, scaled by the ratio of the probability during the expansion and recovery phases combined to the probability at other times averaged between 6 and 15 MLT. These ratios are found to be 1.52 at LER and 1.09 at ESK and HAD. The other component (dark orange) is the residual, which is mostly concentrated in the 17–24 MLT sector. Summing each probability variation over all MLT, we find that at LER the 55% of all large *R* occurring during the expansion and recovery phases combined (cf. the discussion of Figure 4 in section 3.3) is composed of 41% with the same MLT variation as during other times and 14% which varies differently and peaks premidnight (i.e., the residual). At ESK these percentages are 49%, 38%, and 11%, respectively, and at HAD they are 49%, 39%, and 10%. Or put another way, the residual accounts for 25% at LER (i.e., =14%/55%), 23% at ESK, and 21% at HAD of large *R* occurring during the expansion and recovery phases combined.

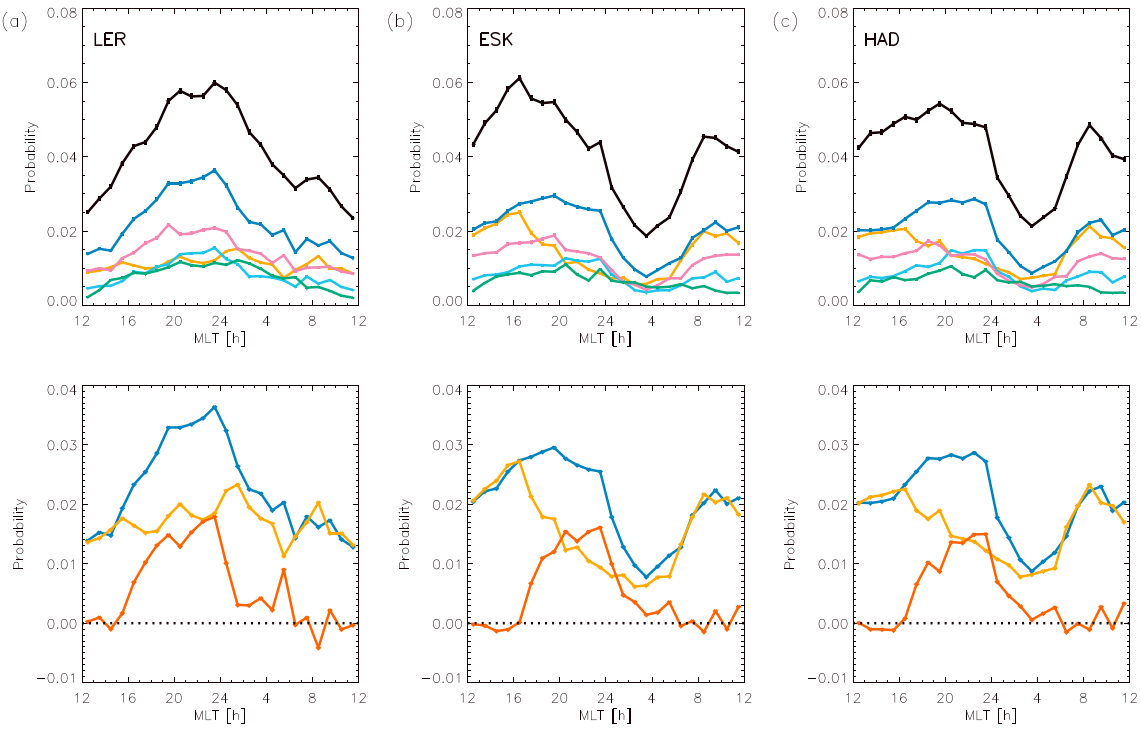

Figure 6. (a–c) Top row: The probability of R exceeding the 99th percentile for the LER, ESK, and HAD magnetic observatories for the interval 1996–2014 inclusive as a function of magnetic local time (MLT) during the expansion phase (sky blue), recovery phase (purple), expansion and recovery phases combined (blue), enhanced convection (green), other times (orange), and overall (black). Bottom row: Decomposition of the probability during the expansion and recovery phases combined (blue) into two components. The first component (orange) is proportional to the probability at other times, scaled by ratios 1.52 at LER and 1.09 at ESK and HAD. The other component (dark orange) is the residual. LER = Lerwick; ESK = Eskdalemuir; HAD = Hartland; MLT = magnetic local time.

4. Discussion

We have analyzed the statistics of the rate of change R of the horizontal component of the surface magnetic field at three U.K. locations and whether and how this is influenced by the substorm. The motivation for the study is to understand the potential role of the substorm in causing hazardous GIC, specifically in respect to the U.K.'s National Grid. Hazardous GIC have been associated with $\partial\mathbf{H}/\partial t$ of hundreds of nanoTesla per minute which are so rare that, even with the 19 years of data used here, the sample size is too small to draw conclusions on influencing factors. For example, only four values of R exceed 600 nT/min at LER, two values at ESK, and none at HAD. Consequently, our analyses have focused on the statistical properties of large and extreme R, which we define as above the 99th and 99.97th percentiles, respectively, in order to identify likely physical sources and asymptotic behaviors.

4.1. Sources of Large and Extreme R

4.1.1. Substorm

We have provided the first quantitative evidence that large and extreme R in the United Kingdom mostly occur during substorm expansion and recovery phases, compared to enhanced convection intervals and other times (see section 3.3). Even though substorm expansion and recovery phases accounted for just 13.4% of our data set, we have found (Figure 4) that about half of all large and extreme R occur during these times. Specifically, depending on the magnetometer station, 49–55% of all large R and 54–56% of extreme R occur during substorm expansion and recovery phases.

Referring to Figure 4, this proportion appears to increase rapidly up to the large R threshold but then not to increase much more up to the extreme R threshold. Beyond this, statistical uncertainties are too large to be sure of the asymptotic tendency. Instead, we note that as R increases from large to extreme, the proportion of R during enhanced convection intervals increases from 15–19% (depending on station) to 30–32%, while the proportion during other times decreases from 27–36% to 12–16%. Thus, it is possible that enhanced

convection intervals become an increasingly important source as R gets even more extreme, potentially rivalling the substorm. Whether this is so is an important focus for future study, not least because substorms are currently unpredictable whereas enhanced convection is probably more predictable.

When normalized by the duration of the different data subsets (Figure 5), it is clear that large and extreme R is much more likely to occur when in the substorm expansion and recovery phases or during enhanced convection intervals than at other times. R at the 99th percentile is 8–10 times more likely to occur when in the substorm expansion and recovery phases than at other times, increasing to 15–30 times more likely for R at the 99.97th percentile. These ratios are even higher during enhanced convection intervals, though it must be remembered that these intervals relatively rare (comprising 1.7% of the total data set) compared with substorm expansion and recovery phases (13.4% combined).

Comparing large R occurrence between the expansion and recovery phases, we find that large R is around 50% more likely in the expansion phase (Figure 5) but overall about 50% more numerous during the recovery phase (Figure 4) because over twice the time is spent in the recovery phase. This is consistent with the analyses of Turnbull et al. (2009) and Viljanen et al. (2006) who showed that the maximum $\partial\mathbf{H}/\partial t$ within an interval from just before substorm onset to 60–90 min afterward preferentially occurs within about 10 min after onset (during the expansion phase) but can occur at any time within the 60-90 min after substorm onset (which would include both the expansion and the longer recovery phase). Importantly, we have now extended their studies to compare this postonset occurrence to that at other times.

As noted in section 2, the numbers given above for the substorm contribution to large and extreme R occurrence are expected to be lower bounds because we have chosen a conservative value of the free parameter EPT that defines the expansion phase in the SOPHIE method. Consequently, some large R instances may have been wrongly identified to occur at other times rather than during the expansion and recovery phases. Specifically, we chose $EPT = 90$ rather than the recommended $EPT = 75$ (Forsyth et al., 2015). Besides being conservative, another rationale for this choice is that decreasing EPT increases the number of intervals identified as expansion phases (from an average of 1,255 per year for $EPT = 90$ to 2,417 for $EPT = 75$ to 3,503 for $EPT = 50$) but does not monotonically change the number of expansion phase onsets preceded by a possible growth phase (1,004 per year for $EPT = 90$ to 1,384 for $EPT = 75$ to 982 for $EPT = 50$). It seems reasonable to suppose that expansion phases preceded by a possible growth phase are classical substorm onsets, whereas the remaining expansion phases preceded by a recovery phase are postonset intensifications of $|SML|$. Consequently, with this interpretation, choosing $EPT = 90$ rather than a lower value preferentially selects substorm expansion phases (i.e., following a possible growth phase) and minimizes other intensification-related expansion phases (i.e., following a recovery phase). The resulting average of 1,255 expansion phases per year (or 1,004 postgrowth expansion phases per year) between 1996 and 2014 is similar to other estimates of the annual number of substorm onsets, such as the study of Chu et al. (2015) which we estimate finds an average of about 1,300 onsets per year over nearly the same interval (1996–2012). Thus, we believe that our choice of $EPT = 90$ is preferable for identifying the influence on R of the substorm as it is classically defined. In any event, we reiterate that our conservative choice provides at worst a lower bound for the effects of the substorm on large and extreme R occurrence.

As an aside, we can also infer that the substorm expansion phase onsets must typically be more rapid changes in $|SML|$ than postonset intensifications because their occurrence is relatively insensitive to varying EPT.

4.1.2. Substorm DP1

Additional evidence for a substorm source was provided in section 3.4 by the analysis of the probability of large R with MLT. In Figure 6 we showed that the overall variation at LER varies fairly smoothly from a minimum at noon MLT to a maximum at 20–24 MLT, whereas at ESK and HAD it is a minimum near 3 MLT and has peaks at 8 MLT and at 16 or 19 MLT, respectively. By comparison, Juusola et al. (2015) report an MLT variation for the same percentile of $\partial\mathbf{H}/\partial t$, which has a broad minimum at 11–16 MLT and peaks at about 5 and 22 MLT. Their data came mostly from higher latitudes (>63° CGM latitude) and so these differences in MLT variation likely reflect how the relative contributions to large $\partial\mathbf{H}/\partial t$ from different current systems change with latitude.

To investigate this, we noted that for all three U.K. observatories the probability of large R during the substorm expansion and recovery phases is enhanced with respect to that at other times in the nightside. This

led us to demonstrate that the MLT variation of the probability of large *R* during the substorm expansion and recovery phases could be decomposed into a component with the same MLT variation as during other times and another component which varies differently with MLT and peaks premidnight. This latter component thus only occurs during the expansion and recovery phases and has an MLT extent between about 16 and 05 MLT that is similar to that of the DP1 magnetic perturbation of the SCW electrojet (e.g., Shore et al., 2018). These facts give us little doubt that this component of large *R* is attributable to large and rapid fluctuations in DP1. It has been suggested that during intense geomagnetic storms the SCW moves to later MLT (Ohtani et al., 2018), but lack of data precludes us from reliably extending our statistical MLT analysis to extreme R.

We found that this DP1 component contributes 14% of all large *R* at LER, 11% at ESK, and 10% at HAD. As a percentage of large *R* occurrence during the substorm expansion and recovery phases alone, the DP1 component contributes 25% at LER, 23% at ESK, and 21% at HAD. Given that DP1 is a defining feature of the substorm, it is perhaps surprising that only a small minority of large *R* are directly attributable to DP1.

4.1.3. DP2

The remaining 75–79% of large *R* perturbations during the expansion and recovery phases are distributed over all MLT and have the same MLT variation as during other times but are more likely to occur than during other times (excluding enhanced convection intervals; see section 3.3). This indicates that the current source of these large *R* is (a) large scale, (b) ubiquitous, but (c) enhanced during the expansion and recovery phases with respect to other times. The magnetosphere-ionosphere current system associated with the DP2 perturbation of the surface magnetic field is consistent with these properties:

(a) DP2 is large scale, comprising a surface magnetic field perturbation over the entire high-latitude ionosphere (Shore et al., 2017, 2018). However, DP2 **H** is strongest in the auroral oval and peaks around 3 and 17 MLT, which is different to the occurrence of non-DP1 large *R* seen in the lower panels of Figure 6: At LER, this is a maximum at midnight MLT and minimum at noon MLT, and at ESK and HAD it peaks at 8 and 16 MLT and is a minimum near 3 MLT. Such an inconsistency could be because the directional distribution of $\partial\mathbf{H}/\partial t$ is known to be more scattered than that of **H** due to mesoscale fluctuations in the ionosphere (Viljanen et al., 2001). In this case, a local correspondence between **H** caused by DP2 and *R* caused by mesoscale fluctuation of DP2 would not be expected. Instead, we would expect the magnitude of *R* to be proportional to the global strength of DP2 because the mesoscale fluctuations are thought to arise from a turbulent cascade of the global-scale eddies of the two-cell ionospheric convection associated with DP2 (Abel et al., 2006, 2007, 2009). The magnitude of *R* would also be expected to decrease with increasing latitudinal distance from the DP2 electrojets, in which the mesoscale fluctuations are concentrated. This would explain the MLT variation of the probability of large *R* at LER, which, being a typically subauroral station, is closest to the auroral oval at midnight MLT and furthest away at noon MLT because the oval is tilted by several degrees antisunward (Holzworth & Meng, 1975). In fact, at high geomagnetic disturbance level, $Kp = 8$, it is estimated (Carbary, 2005) that LER varies from well inside the auroral oval at midnight MLT (i.e., 5.9° poleward of its equatorward edge) to just outside it (i.e., 1.5° equatorward) at 14 MLT (noon MLT data are not available). By comparison, ESK varies from 0.5° inside to 6.9° outside and HAD varies from 4.6° to 12° outside.

(b) DP2, and hence the mesoscale turbulence within it, is sustained by the trans-polar voltage created by the motional electric field of the solar wind across open magnetic field lines which are ever present (e.g., Lockwood et al., 1990). Furthermore, DP2 is known to always be the largest contributor to monthly variance of the surface magnetic field (Shore et al., 2018), and so DP2 turbulence could cause large *R* at any time.

(c) DP2 is stronger during the substorm expansion and recovery phases than at other times because (i) the transpolar voltage is positively correlated with southward IMF (e.g., Haaland et al., 2007; Reiff et al., 1981) and southward IMF is also a necessary condition for substorm onset (e.g., Freeman & Morley, 2009) and (ii) substorms generally enhance ionospheric conductivity during the expansion and recovery phases (Aksnes et al., 2002; Gjerloev & Hoffman, 2000a, 2000b) producing stronger ionospheric currents and hence *R* for a given voltage.

In summary, non-DP1 large *R* during the substorm expansion and recovery phases could be caused by mesoscale fluctuations of DP2 (despite DP2 **H** having a different MLT variation). Note also that enhanced convection intervals are defined by rapidly and approximately equally increasing eastward and westward

electrojet strengths, consistent with strong DP2 (see section 2.4). Thus, the above arguments may then similarly explain the importance of enhanced convection intervals to the occurrence of large and extreme *R* (Figures 4 and 5).

4.1.4. Sudden Commencement

Another possible source of non-DP1 large *R* is from Sudden Impulses and Sudden Storm Commencements, collectively known as geomagnetic Sudden Commencements (SC) (Fiori et al., 2014). These are caused by compression of the magnetosphere when an interplanetary shock passes the Earth. Consequently, like DP2, SC are large scale and can occur both during substorms and at other times. At the Earth's surface, an SC comprises two components—DL and DP, giving rise to a complicated variation with latitude and MLT of the surface **H** signature (Araki, 1994), and consequently of *R* (Carter et al., 2016; Fiori et al., 2014).

DL is the purely compressional perturbation of the surface magnetic field caused by the enhancement of the magnetopause current confining the compressed magnetosphere. Theoretically and observationally, the compressional perturbation for a given solar wind dynamic pressure change is highest at noon MLT and decreases toward midnight MLT (Kokubun, 1983; Russell et al., 1992). This may partly explain the higher probability of large *R* during daytime MLT at ESK and HAD (but not the opposite tendency at LER that we have associated with latitudinal proximity to the auroral zone currents; see 4.1.3 above). However, DL is only expected to be dominant between 15° and 30° CGM latitude during northward IMF (Russell et al., 1992).

Otherwise, the DP component is important. This is caused by coupling of the magnetospheric compression to shear Alfvén waves and field-aligned resonances (Farrugia et al., 1989; Lysak & Lee, 1992; Southwood & Kivelson, 1990), causing so-called travelling convection vortices (TCV; Friis-Christensen et al., 1988) that propagate away westward and eastward from noon MLT and whose strength maximizes around 9 MLT (Moretto et al., 1997). In contrast to the purely compressional SC, the strength of the TCV-associated localized surface magnetic field perturbations will be influenced by ionospheric conductivity from a combination of both solar illumination and particle precipitation (Hartinger et al., 2017). Thus, the DP component might contribute to the dayside enhancement in large *R* seen at ESK and HAD and possibly the peaks at 8 and 16 MLT that are symmetric about the origin of TCV propagation at noon MLT. As with DP2, the dependence on conductivity could contribute to the greater probability of large *R* during the substorm expansion and recovery phases compared with other times.

4.1.5. Storm Time Pc5 Waves

Another possible Alfvén wave source of large *R* is Pc5 pulsations caused by the Kelvin-Helmholtz instability and overreflection of waveguide modes at the magnetopause (e.g., Mann et al., 1999; and references therein). This is associated with dawnside, and sometimes also duskside, peaks in wave power which might be associated with the 8 and 16 MLT peaks in large *R*. Such pulsations are not usually considered as a GIC source. However, a 4-min period Pc5 wave of amplitude *A* nT would correspond to $R \sim A$ nT/min and so waves exceeding the large *R* threshold of say 6.8 nT/min at ESK would not be exceptional. Furthermore, Pc5 power increases with solar wind speed (Mathie & Mann, 2001) and so by extrapolation it is conceivable that Pc5 waves could become of sufficiently large amplitude to produce extreme *R* during say magnetic storms caused by high-speed solar wind streams. Indeed, a study by Marin et al. (2014) has shown that at midlatitude and auroral zone magnetometers during the recovery phase of the Halloween magnetic storm high wave powers occurred in both the morning and afternoon MLT with rates of change corresponding to $R \sim 100$ nT/min, above the extreme *R* threshold in the United Kingdom.

In summary, we suggest that while large and extreme *R* are most prevalent during the substorm and expansion phases, they are caused by various physical sources besides the SCW. The separation and relative importance of these will be investigated further in future studies.

4.2. Implications for the National Grid

As mentioned earlier, the purpose of this study is to understand the possible factors influencing relatively common large *R* and extreme *R* in the United Kingdom in order to extrapolate to the rare hazardous *R* (>600 nT/min) that may adversely affect the U.K.'s National Grid.

From a simple overall risk assessment point of view, just over half of all instances of extreme *R* in the United Kingdom occurred during the substorm expansion and recovery phases (sections 3.3 and 4.1.1).

An additional third of extreme R occur during enhanced convection intervals. The proportion of R occurring during other times appears to monotonically decrease with increasing R (Figure 4), and so it seems clear that substorm expansion and recovery phases and enhanced convection intervals are the two important influences on the hazardous R that may damage the National Grid. However, the trend in the relative importance of these two influences is uncertain. The importance of enhanced convection systematically increases between the large and extreme R thresholds but then appears to plateau or even decrease at larger R. This would suggest that the substorm expansion and recovery phases remain the most important influence for hazardous R. However, the low occurrence frequencies of R in this region make the statistical uncertainties too high to be certain of this tendency. If instead the trend seen between large and extreme R thresholds continued then this could imply that enhanced convection intervals become as important as substorm expansion and recovery phases as the source of hazardous R.

From a nowcasting perspective, we can conclude that if observations tell us that a substorm onset has occurred and we are in the expansion or recovery phase then, in the absence of other information, we estimate that the probability of extreme R is increased by ~10 compared to other times (Figure 5). Of course, other information, such as substorm size, might well influence the relative probability of extreme R, but this has not been investigated here (e.g., Weimer, 1994, provides evidence that the post onset rate of change of the lower auroral electrojet index AL increases with peak AL). In Figure 5, the ratio of the PDF of R during the expansion and recovery phases compared to other times is roughly a power law over the statistically reliable (i.e., continuous curve) region above the large R threshold. Simple extrapolation of the best fit (shown by the dashed black line) indicates that the PDF ratio rises to ~100 at the hazardous R ~ 600-nT/min threshold. Similarly, the probability of extreme R is increased by a factor of ~100 during enhanced convection intervals compared to other times and extrapolates (dotted black line) to ~1,000 for R ~ 600 nT/min. The divergence of the substorm and enhanced convection trends would then indicate an ultimately asymptotic dominance of enhanced convection intervals as the source of hazardous R. However, as with the discussion of Figure 4, simple extrapolation is questionable and is primarily to demonstrate a possibility rather than a fact.

From a forecasting perspective, the majority influence of the substorm on extreme R occurrence seems problematic because, as discussed in section 1, it is not currently possible to forecast the timing of substorm onset and the size of DP1 because they are almost certainly nonlinear time-integrated properties of the interplanetary state that are not fully known and likely have chaotic properties (e.g., Freeman & Farrugia, 1999; Freeman & Morley, 2004; Morley et al., 2007, 2009). However, if the aforementioned asymptotic dominance of enhanced convection intervals as the source of hazardous R is true, then the forecasting prospects at this higher level of R are improved. This is because, almost by definition, DP2 is surely dominant during enhanced convection intervals and DP2 is more predictable than DP1 from interplanetary observations (e.g., Shore et al., 2018). Even if this were not true and hazardous R mostly occurs during substorm expansion and recovery phases, our decomposition of large R by MLT showed that DP1 is a minor influence on large R occurrence and that amplification of DP2 variations during the expansion and recovery phase, and possibly also of SC, is why the substorm is such an important influence on large R. From this, it seems likely that our ability to understand and forecast DP2 rather than DP1 is the key to forecasting hazardous R, recognizing however that the substorm feedback on ionospheric conductivity may be important for understanding DP2. This will be another focus of future work.

While this study has concentrated in the United Kingdom, we expect similar properties of large and extreme R at other locations with similar geomagnetic latitude, though differences could arise from local geology affecting the contribution to $\mathbf{H}$ and hence, R, from currents induced in the ground (e.g., Tanskanen et al., 2001). For example, the estimated 100-year return levels of $\partial\mathbf{H}/\partial t$ at HAD and LER are not significantly different to those at approximately the same (uncorrected) geomagnetic latitudes in Canada (observatories VIC and MEA, respectively), whereas the return level at ESK is anomalously higher than at a similar latitude in Canada (GLN or STJ) and also higher than HAD or LER on either latitudinal side of ESK (Nikitina et al., 2016; Thomson et al., 2011). Systematic differences would also be expected with varying geomagnetic latitude (e.g., Juusola et al., 2015; Nikitina et al., 2016; Thomson et al., 2011), and this was indeed observed between the three U.K. magnetic observatories studied here (e.g., Figures 3 and 6). Consequently, we intend to extend our analysis to other locations.

Furthermore, as mentioned in section 1, knowledge of R is a necessary but insufficient condition for understanding the impact on an electricity supply network. Thus, we intend our results to be used in conjunction with other information (e.g., network architecture and ground conductivity) to deduce the all-important GICs.

5. Conclusions

We have shown that the large and extreme rates of change R in the horizontal component of the surface magnetic field at three U.K. locations (LER, ESK, and HAD) are strongly influenced by the substorm. Large refers to above the 99th percentile and extreme to above the 99.97th percentile. Key facts are as follows:

- Our analysis finds that 56% of all extreme R values at LER occur during the substorm expansion or recovery phases and 54% at both ESK and HAD. These may be underestimates because a conservative definition of the substorm was used.
- The MLT variation of large R occurrence at LER indicates that only 25% of large R values during the substorm expansion or recovery phases are attributable to the DP1 magnetic perturbation caused by the SCW. This corresponds to 14% of all large R. The corresponding numbers are 23% and 11% at ESK and 21% and 10% at HAD. Other candidate sources of large R are DP2, SC, and storm time Pc5 waves.
- Given that an observation is during the expansion or recovery phase, the occurrence probability of R at the 99.97th percentile is increased by ~10 compared to other times. Based on simple extrapolation of the approximately power law trend between large and extreme R, this factor rises to ~100 for R ~ 600 nT/min.
- Similarly, the occurrence probability of R at the 99.97th percentile is increased by a factor of ~100 during enhanced convection intervals compared to other times and extrapolates to ~1,000 for R ~ 600 nT/min.
- The above results suggest DP2 as the dominant source of hazardous $R > 600$ nT/min that is potentially damaging to the U.K. National Grid.

We conclude that further research is needed to understand and model DP2, its mesoscale turbulent structure, and substorm feedbacks on it in order that GIC impact on the U.K. National Grid may be better understood and predicted.

Acknowledgments
The author thanks Gemma Richardson for providing Figure 1 and Alan Thomson for helpful suggestions and comments. The results presented in this paper rely on the data collected at the Eskdalemuir, Hartland, and Lerwick observatories. We thank the British Geological Survey for supporting their operation and INTERMAGNET for promoting high standards of magnetic observatory practice. The data were downloaded from www.intermagnet.org and are freely available there. Corrected geomagnetic coordinates given in section 2 were calculated on 31 July 2018 using the online calculator at https://omniweb.sci.gsfc.nasa.gov/vitmo/cgm.html, and sunspot data were retrieved on 31 July 2018 from the WDC-SILSO, Royal Observatory of Belgium, Brussels, at their website (http://sidc.oma.be/silso/datafiles). Carrington rotation dates were downloaded on 11 October 2018 from http://umtof.umd.edu/pm/crn/, courtesy of the CELIAS/MTOF experiment team of the Solar Heliospheric Observatory (SOHO) spacecraft. M. P. F. and I. J. R. were supported by U.K. Natural Environment Research Council (NERC) grants NE/P016693/1 and NE/P017150/1, respectively. C. F. was supported by NERC Independent Research Fellowship NE/N014480/2.

References

Abel, G., Freeman, M. P., Chisham, G., & Watkins, N. W. (2007). Investigating turbulent structure of ionospheric plasma velocity using the Halley SuperDARN radar. *Nonlinear Processes in Geophysics*, *14*(6), 799–809. https://doi.org/10.5194/npg-14-799-2007

Abel, G. A., Freeman, M. P., & Chisham, G. (2006). Spatial structure of ionospheric convection velocities in regions of open and closed magnetic field topology. *Geophysical Research Letters*, *33*, L24103. https://doi.org/10.1029/2006GL027919

Abel, G. A., Freeman, M. P., & Chisham, G. (2009). IMF clock angle control of multifractality in ionospheric velocity fluctuations. *Geophysical Research Letters*, *36*, L19102. https://doi.org/10.1029/2009GL040336

Akasofu, S.-I. (1964). The development of the auroral substorm. *Planetary and Space Science*, *12*(4), 273–282. https://doi.org/10.1016/0032-0633(64)90151-5

Aksnes, A., Stadsnes, J., Bjordal, J., Østgaard, N., Vondrak, R. R., Detrick, D. L., et al. (2002). Instantaneous ionospheric global conductance maps during an isolated substorm. *Annales Geophysicae*, *20*(8), 1181–1191. https://doi.org/10.5194/angeo-20-1181-2002

Araki, T. (1994). A physical model of the geomagnetic sudden commencement. *Geophysical Monograph*, *81*, 183–200.

Beggan, C. D. (2015). Sensitivity of geomagnetically induced currents to varying auroral electrojet and conductivity models. *Earth, Planets and Space*, *67*(24), 1–12. https://doi.org/10.1186/s40623-014-0168-9

Borovsky, J. E., & Denton, M. H. (2006). Differences between CME-driven storms and CIR-driven storms. *Journal of Geophysical Research*, *111*, A07S08. https://doi.org/10.1029/2005JA011447

Cannon, P., Angling, M., Barclay, L., Curry, C., Dyer, C., Edwards, R., et al. (2013). *Extreme space weather: Impacts on engineered systems and infrastructure*. London: Royal Academy of Engineering.

Carbary, J. F. (2005). A Kp-based model of auroral boundaries. *Space Weather*, *3*, S10001. https://doi.org/10.1029/2005sw000162

Carter, B. A., Yizengaw, E., Pradipta, R., Weygand, J. M., Piersanti, M., Pulkkinen, A., et al. (2016). Geomagnetically induced currents around the world during the 17 March 2015 storm. *Journal of Geophysical Research: Space Physics*, *121*, 10,496–10,507. https://doi.org/10.1002/2016JA023344

Chu, X., McPherron, R. L., Hsu, T.-S., & Angelopoulos, V. (2015). Solar cycle dependence of substorm occurrence and duration: Implications for onset. *Journal of Geophysical Research: Space Physics*, *120*, 2808–2818. https://doi.org/10.1002/2015JA021104

Coxon, J. C., Freeman, M. P., Jackman, C. M., Forsyth, C., Rae, I. J., & Fear, R. C. (2018). Tailward propagation of magnetic energy density variations with respect to substorm onset times. *Journal of Geophysical Research: Space Physics*, *123*, 4741–4754. https://doi.org/10.1029/2017JA025147

Dungey, J. W. (1961). Interplanetary magnetic field and the auroral zones. *Physical Review Letters*, *6*(2), 47–48. https://doi.org/10.1103/PhysRevLett.6.47

Erinmez, I. A., Kappenman, J. G., & Radasky, W. A. (2002). Management of the geomagnetically induced current risks on the national grid company's electric power transmission system. *Journal of Atmospheric and Solar-Terrestrial Physics*, *64*(5-6), 743–756. https://doi.org/10.1016/S1364-6826(02)00036-6

Farrugia, C. J., Freeman, M. P., Cowley, S. W. H., Southwood, D. J., Lockwood, M., & Etemadi, A. (1989). Pressure-driven magnetopause motions and attendant response on the ground. *Planetary and Space Science*, *37*(5), 589–607. https://doi.org/10.1016/0032-0633(89)90099-8

Fiori, R. A. D., Boteler, D. H., & Gillies, D. M. (2014). Assessment of GIC risk due to geomagnetic sudden commencements and identification of the current systems responsible. *Space Weather*, *12*, 76–91. https://doi.org/10.1002/2013SW000967

Forsyth, C., Rae, I. J., Coxon, J. C., Freeman, M. P., Jackman, C. M., Gjerloev, J., & Fazakerley, A. N. (2015). A new technique for determining Substorm Onsets and Phases from Indices of the Electrojet (SOPHIE). *Journal of Geophysical Research: Space Physics*, *120*, 10,592–10,606. https://doi.org/10.1002/2015JA021343

Forsyth, C., Watt, C. E. J., Rae, I. J., Fazakerley, A. N., Kalmoni, N. M. E., Freeman, M. P., et al. (2014). Increases in plasma sheet temperature with solar wind driving during substorm growth phases. *Geophysical Research Letters*, *41*, 8713–8721. https://doi.org/10.1002/2014GL062400

Freeman, M. P., & Farrugia, C. J. (1999). Solar wind input between substorm onsets during and after the October 18-20, 1995, magnetic cloud. *Journal of Geophysical Research*, *104*(A10), 22,729–22,744. https://doi.org/10.1029/1999JA900204

Freeman, M. P., & Morley, S. K. (2004). A minimal substorm model that explains the observed statistical distribution of times between substorms. *Geophysical Research Letters*, *31*, L12807. https://doi.org/10.1029/2004GL019989

Freeman, M. P., & Morley, S. K. (2009). No evidence for externally triggered substorms based on superposed epoch analysis of IMF Bz. *Geophysical Research Letters*, *36*, L21101. https://doi.org/10.1029/2009GL040621

Friis-Christensen, E., McHenry, M. A., Clauer, C. R., & Vennerstrøm, S. (1988). Ionospheric traveling convection vortices observed near the polar cleft: A triggered response to sudden changes in the solar wind. *Geophysical Research Letters*, *15*(3), 253–256. https://doi.org/10.1029/GL015i003p00253

Friis-Christensen, E., & Wilhjelm, J. (1975). Polar cap currents for different directions of the interplanetary magnetic field in the Y-Z plane. *Journal of Geophysical Research*, *80*(10), 1248–1260. https://doi.org/10.1029/JA080i010p01248

Gehrels, N. (1986). Confidence limits for small numbers of events in astrophysical data. *The Astrophysical Journal*, *303*, 336–346.

Gjerloev, J. W. (2012). The SuperMAG data processing technique. *Journal of Geophysical Research*, *117*, A09213. https://doi.org/10.1029/2012JA017683

Gjerloev, J. W., & Hoffman, R. A. (2000a). Height-integrated conductivity in auroral substorms 1. Data. *Journal of Geophysical Research*, *105*(A1), 227–235. https://doi.org/10.1029/1999JA900354

Gjerloev, J. W., & Hoffman, R. A. (2000b). Height-integrated conductivity in auroral substorms 2. Modeling. *Journal of Geophysical Research*, *105*(A1), 215–226. https://doi.org/10.1029/1999JA900353

Gordeev, E., Sergeev, V., Tsyganenko, N., Kuznetsova, M., Rastäetter, L., Raeder, J., et al. (2017). The substorm cycle as reproduced by global MHD models. *Space Weather*, *15*, 131–149. https://doi.org/10.1002/2016SW001495

Haaland, S. E., Paschmann, G., Förster, M., Quinn, J. M., Torbert, R. B., McIlwain, C. E., et al. (2007). High-latitude plasma convection from Cluster EDI measurements: method and IMF-dependence. *Annales Geophysicae*, *25*(1), 239–253. https://doi.org/10.5194/angeo-25-239-2007

Harrison, R. A., Davies, J. A., Biesecker, D., & Gibbs, M. (2017). The application of heliospheric imaging to space weather operations: Lessons learned from published studies. *Space Weather*, *15*, 985–1003. https://doi.org/10.1002/2017SW001633

Hartinger, M. D., Xu, Z., Clauer, C. R., Yu, Y., Weimer, D. R., Kim, H., et al. (2017). Associating ground magnetometer observations with current or voltage generators. *Journal of Geophysical Research: Space Physics*, *122*, 7130–7141. https://doi.org/10.1002/2017JA024140

Holzworth, R. H., & Meng, C.-I. (1975). Mathematical representation of the auroral oval. *Geophysical Research Letters*, *2*(9), 377–380. https://doi.org/10.1029/GL002i009p00377

Hones, E. W. Jr. (1979). Transient phenomena in the magnetotail and their relation to substorms. *Space Science Reviews*, *23*(3), 393–410. https://doi.org/10.1007/BF00172247

Huang, C. S., Le, G., & Reeves, G. D. (2004). Periodic magnetospheric substorms during fluctuating interplanetary magnetic field Bz. *Geophysical Research Letters*, *31*, L14801. https://doi.org/10.1029/2004GL020180

Juusola, L., Viljanen, A., van de Kamp, M., Tanskanen, E. I., Vanhamäki, H., Partamies, N., & Kauristie, K. (2015). High-latitude ionospheric equivalent currents during strong space storms: Regional perspective. *Space Weather*, *13*, 49–60. https://doi.org/10.1002/2014SW001139

Kalmoni, N. M. E., Rae, I. J., Murphy, K. R., Forsyth, C., Watt, C. E. J., & Owen, C. J. (2017). Statistical azimuthal structuring of the substorm onset arc: Implications for the onset mechanism. *Geophysical Research Letters*, *44*, 2078–2087. https://doi.org/10.1002/2016GL071826

Kalmoni, N. M. E., Rae, I. J., Watt, C. E. J., Murphy, K. R., Forsyth, C., & Owen, C. J. (2015). Statistical characterization of the growth and spatial scales of the substorm onset arc. *Journal of Geophysical Research: Space Physics*, *120*, 8503–8516. https://doi.org/10.1002/2015JA021470

Kalmoni, N. M. E., Rae, I. J., Watt, C. E. J., Murphy, K. R., Samara, M., Michell, R. G., et al. (2018). A diagnosis of the plasma waves responsible for the explosive energy release of substorm onset. *Nature Communications*, *9*(1), 4806. https://doi.org/10.1038/s41467-018-07086-0

Kokubun, S. (1983). Characteristics of storm sudden commencement at geostationary orbit. *Journal of Geophysical Research*, *88*(12), 10,025–10,033. https://doi.org/10.1029/JA088iA12p100

Lee, D.-Y., Lyons, L. R., Kim, K. C., Baek, J.-H., Kim, K. H., Kim, H. J., et al. (2006). Repetitive substorms caused by Alfvénic waves of the interplanetary magnetic field during high-speed solar wind streams. *Journal of Geophysical Research*, *111*, A12214. https://doi.org/10.1029/2006JA011685

Lehtinen, M., & Pirjola, R. (1985). Currents produced in earthed conductor networks by geomagnetically-induced electric fields. *Annales Geophysicae*, *3*, 479–484.

Lockwood, M., Cowley, S. W. H., & Freeman, M. P. (1990). The excitation of plasma convection in the high-latitude ionosphere. *Journal of Geophysical Research*, *95*(A6), 7961–7972. https://doi.org/10.1029/JA095iA06p07961

Love, J. J., & Gannon, J. L. (2009). Revised Dst and the epicycles of magnetic disturbance: 1958–2007. *Annales Geophysicae*, *27*(8), 3101–3131. https://doi.org/10.5194/angeo-27-3101-2009

Love, J. J., Lucas, G. M., Kelbert, A., & Bedrosian, P. A. (2018). Geoelectric hazard maps for the Mid-Atlantic United States: 100 year extreme values and the 1989 magnetic storm. *Geophysical Research Letters*, *45*, 5–14. https://doi.org/10.1002/2017GL076042

Lysak, R. L., & Lee, D.-H. (1992). Response of the dipole magnetosphere to pressure pulses. *Geophysical Research Letters*, *19*(9), 937–940. https://doi.org/10.1029/92GL00625

Mann, I. J., Wright, A. N., Mills, K. J., & Nakariakov, V. M. (1999). Excitation of magnetospheric waveguide modes by magnetosheath flows. *Journal of Geophysical Research*, *104*(A1), 333–353. https://doi.org/10.1029/1998JA900026

Marin, J., Pilipenko, V., Kozyreva, O., Stepanova, M., Engebretson, M., Vega, P., & Zesta, E. (2014). Global Pc5 pulsations during strong magnetic storms: excitation mechanisms and equatorward expansion. *Annales Geophysicae*, *32*(4), 319–331. https://doi.org/10.5194/angeo-32-319-2014

Mathie, R. A., & Mann, I. R. (2001). On the solar wind control of Pc5 ULF pulsation power at mid-latitudes—Implications for MeV electron acceleration in the outer radiation belt. *Journal of Geophysical Research*, *106*(A12), 29,783–29,796. https://doi.org/10.1029/2001JA000002

McPherron, R. L. (1970). Growth phase of magnetospheric substorms. *Journal of Geophysical Research*, *75*(28), 5592–5599. https://doi.org/10.1029/JA075i028p05592

McPherron, R. L., Russell, C. T., & Aubry, M. P. (1973). Satellite studies of magnetospheric substorms on August 15, 1968: 9. Phenomenological model for substorms. *Journal of Geophysical Research*, *78*(16), 3131–3149. https://doi.org/10.1029/JA078i016p03131

Moretto, T., Friis-Christensen, E., Luhr, H., & Zesta, E. (1997). Global perspective of ionospheric traveling convection vortices: Case studies of two Geospace Environmental Modeling events. *Journal of Geophysical Research*, *102*(A6), 11,597–11,610. https://doi.org/10.1029/97JA00324

Morley, S. K., Freeman, M. P., & Tanskanen, E. I. (2007). A comparison of the probability distribution of observed substorm magnitude with that predicted by a minimal substorm model. *Annales Geophysicae*, *25*(11), 2427–2437. https://doi.org/10.5194/angeo-25-2427-2007

Morley, S. K., Rouillard, A. P., & Freeman, M. P. (2009). Recurrent substorm activity during the passage of a corotating interaction region. *Journal of Atmospheric and Solar-Terrestrial Physics*, *71*(10-11), 1073–1081. https://doi.org/10.1016/j.jastp.2008.11.009

Nikitina, L., Trichtchenko, L., & Boteler, D. H. (2016). Assessment of extreme values in geomagnetic and geoelectric field variations for Canada. *Space Weather*, *14*, 481–494. https://doi.org/10.1002/2016SW001386

Nishida, A. (1968a). Geomagnetic D_p 2 fluctuations and associated magnetospheric phenomena. *Journal of Geophysical Research*, *73*(5), 1795–1803. https://doi.org/10.1029/JA073i005p01795

Nishida, A. (1968b). Coherence of geomagnetic DP 2 fluctuations with interplanetary magnetic variations. *Journal of Geophysical Research*, *73*(17), 5549–5559. https://doi.org/10.1029/JA073i017p05549

Ohtani, S., Gjerloev, J. W., Anderson, B. J., Kataoka, R., Troshichev, O., & Watari, S. (2018). Dawnside wedge current system formed during intense geomagnetic storms. *Journal of Geophysical Research: Space Physics*, *123*(11), 9093–9109. https://doi.org/10.1029/2018ja025678

Ostgaard, N., Germany, G., Stadsnes, J., & Vondrak, R. R. (2002). Energy analysis of substorms based on remote sensing techniques, solar wind measurements, and geomagnetic indices. *Journal of Geophysical Research*, *107*(A9), 1233. https://doi.org/10.1029/2001JA002002

Pulkkinen, A., Kuznetsova, M., Ridley, A., Raeder, J., Vapirev, A., Weimer, D., et al. (2011). Geospace environment modeling 2008–2009 challenge: Ground magnetic field perturbations. *Space Weather*, *9*, S02004. https://doi.org/10.1029/2010SW000600

Reiff, P. H., Spiro, R. W., & Hill, T. W. (1981). Dependence of polar cap potential drop on interplanetary parameters. *Journal of Geophysical Research*, *86*(A9), 7639–7648. https://doi.org/10.1029/JA086iA09p07639

Rodger, C. J., MacManus, D. H., Dalzell, M., Thomson, A. W. P., Clarke, E., Petersen, T., et al. (2017). Long-term geomagnetically induced current observations from New Zealand: Peak current estimates for extreme geomagnetic storms. *Space Weather*, *15*, 1447–1460. https://doi.org/10.1002/2017SW001691

Russell, C. T., Ginskey, M., Petrinec, S., & Le, G. (1992). The effect of solar wind dynamic pressure changes on low and mid-latitude magnetic records. *Geophysical Research Letters*, *19*(12), 1227–1230. https://doi.org/10.1029/92GL01161

Sandhu, J. K., Rae, I. J., Freeman, M. P., Forsyth, C., Gkioulidou, M., Reeves, G. D., et al. (2018). Energization of the ring current by substorms. *Journal of Geophysical Research: Space Physics*, *123*, 8131–8148. https://doi.org/10.1029/2018JA025766

Shore, R. M., Freeman, M. P., & Gjerloev, J. W. (2018). An empirical orthogonal function reanalysis of the northern polar external and induced magnetic field during solar cycle 23. *Journal of Geophysical Research: Space Physics*, *123*, 781–795. https://doi.org/10.1002/2017JA024420

Shore, R. M., Freeman, M. P., Wild, J. A., & Gjerloev, J. W. (2017). A high-resolution model of the external and induced magnetic field at the Earth's surface in the Northern Hemisphere. *Journal of Geophysical Research: Space Physics*, *122*, 2440–2454. https://doi.org/10.1002/2016JA023682

Southwood, D. J., & Kivelson, M. G. (1990). The magnetohydrodynamic response of the magnetospheric cavity to changes in solar wind pressure. *Journal of Geophysical Research*, *95*(A3), 2301–2309. https://doi.org/10.1029/JA095iA03p02301

St-Louis, B. (2012). *INTERMAGNET Technical Reference Manual version 4.* (Vol. 6, p. 5). http://intermagnet.org/publications/intermag_4-6.pdf

Tanskanen, E., Pulkkinen, T. I., Koskinen, H. E. J., & Slavin, J. A. (2002). Substorm energy budget during low and high solar activity: 1997 and 1999 compared. *Journal of Geophysical Research*, *107*(A6), 1086. https://doi.org/10.1029/2001JA900153

Tanskanen, E. I., Viljanen, A., Pulkkinen, T. I., Pirjola, R., Häkkinen, L., Pulkkinen, A., & Amm, O. (2001). At substorm onset, 40% of AL comes from underground. *Journal of Geophysical Research*, *106*(A7), 13,119–13,134. https://doi.org/10.1029/2000JA900135

Thomson, A. W. P., Dawson, E. B., & Reay, S. J. (2011). Quantifying extreme behavior in geomagnetic activity. *Space Weather*, *9*, S10001. https://doi.org/10.1029/2011SW000696

Thomson, A. W. P., McKay, A. J., Clarke, E., & Reay, S. J. (2005). Surface electric fields and geomagnetically induced currents in the Scottish Power grid during the 30 October 2003 geomagnetic storm. *Space Weather*, *3*, S11002. https://doi.org/10.1029/2005SW000156

Thomson, D. J., & Weaver, J. T. (1975). The complex image approximation for induction in a multilayered Earth. *Journal of Geophysical Research*, *80*(1), 123–129. https://doi.org/10.1029/JA080i001p00123

Turnbull, K. L., Wild, J. A., Honary, F., Thomson, A. W. P., & McKay, A. J. (2009). Characteristics of variations in the ground magnetic field during substorms at mid latitudes. *Annales Geophysicae*, *27*(9), 3421–3428. https://doi.org/10.5194/angeo-27-3421-2009

Viljanen, A., Amm, O., & Pirjola, R. (1999). Modeling geomagnetically induced currents during different ionospheric situations. *Journal of Geophysical Research*, *104*(A12), 28,059–28,071. https://doi.org/10.1029/1999JA900337

Viljanen, A., Nevanlinna, H., Pajunpää, K., & Pulkkinen, A. (2001). Time derivative of the horizontal geomagnetic field as an activity indicator. *Annales Geophysicae*, *19*(9), 1107–1118. https://doi.org/10.5194/angeo-19-1107-2001

Viljanen, A., Tanskanen, E. I., & Pulkkinen, A. (2006). Relation between substorm characteristics and rapid temporal variations of the ground magnetic field. *Annales Geophysicae*, *24*(2), 725–733. https://doi.org/10.5194/angeo-24-725-2006

Weimer, D. R. (1994). Substorm time constants. *Journal of Geophysical Research*, *99*(A6), 11005. https://doi.org/10.1029/93ja02721

Zhao, X., & Dryer, M. (2014). Current status of CME/shock arrival time prediction. *Space Weather*, *12*, 448–469. https://doi.org/10.1002/2014SW001060